



1 A dataset on the structural diversity of European forests

2

3 Marco Girardello*¹, Gonzalo Oton*¹, Matteo Piccardo² Mark Pickering², Agata Elia², Guido Ceccherini¹,
4 Mariano Garcia³ Mirco Migliavacca¹ Alessandro Cescatti¹

5 ¹European Commission, Joint Research Centre, Italy

6 ²Consultant of European Commission, Joint Research Centre, Italy

7 ³Universidad de Alcalá, Department of Geology, Geography and the Environment, Environmental Remote Sensing Research
8 Group, C/ Colegios, 2, Alcalá de Henares, 28801, Madrid, Spain

9

10 *Correspondence to:* Marco Girardello (marco.girardello@gmail.com), Gonzalo Oton (gonzalo.oton@ec.europa.eu)

11 * These authors contributed equally

12 **Abstract.** Forest structural diversity, defined as the heterogeneity of canopy structural elements in space, is an important axis
13 of functional diversity and is central to understanding the relationship between canopy structure, biodiversity, and ecosystem
14 functioning. Despite the recognised importance of forest structural diversity, the development of specific data products has
15 been hindered by the challenges associated with collecting information on forest structure over large spatial scales. However,
16 the advent of novel spaceborne LiDAR sensors like the Global Ecosystem Dynamics Investigation (GEDI) is now
17 revolutionising the assessment of forest structural diversity by providing high-quality information on forest structural
18 parameters with a quasi-global coverage. Whilst the availability of GEDI data and the computational capacity to handle large
19 datasets have opened up new opportunities for mapping structural diversity, GEDI only collects sparse measurements of
20 vegetation structure. Continuous information of forest structural diversity over large spatial domains may be needed for a
21 variety of applications. The aim of this study was to create wall-to-wall maps of canopy structural diversity in European forests
22 using a predictive modelling framework based on machine learning. We leverage multispectral and Synthetic Aperture Radar
23 (SAR) data to create a series of input features that were related to eight different structural diversity metrics, calculated using
24 GEDI. The models proved to be robust, indicating that active radar and passive optical data can effectively be used to predict
25 structural diversity. Our dataset finds applications in a range of disciplines, including ecology, hydrology, and climate science.
26 As our models can be regularly rerun as new images become available, it can be used to monitor the impacts of climate change
27 and land use management on forest structural diversity.

28



29 **1 Introduction**

30 Information on forest canopy structure is important for several disciplines, including Earth System Science, Ecology,
31 Hydrology, and Climate Science. Forest canopy structure plays a fundamental role in ecosystem functioning by affecting
32 carbon storage and cycling, regulating the hydrological cycle, and influencing local and regional climate patterns (Migliavacca
33 et al., 2021; Shugart et al., 2010; Sun et al., 2018). In addition, canopy structure is critical for maintaining high levels of
34 biodiversity by supporting a high diversity of ecological niches (Larue et al., 2019).

35 The concept of structural diversity or complexity, herein defined as the heterogeneity or variability of canopy structural
36 elements in vertical or horizontal space (Ehbrecht et al., 2021; Hakkenberg et al., 2023; LaRue et al., 2019), is central to
37 understanding the relationship between canopy structure, biodiversity, and ecosystem functioning. Structurally diverse forests
38 can host a wide variety of functionally complementary species, which tend to increase resource-use efficiency and promote
39 feedbacks that enhance resource availability (Gough et al., 2019; Murphy et al., 2022). As a result, these forests can capture
40 light more efficiently, leading to increased ecosystem productivity (Atkins et al., 2018; Toda et al., 2023). Therefore, the
41 availability of data on forest structural diversity over large spatial scales is critical for predicting and managing the response
42 of forest ecosystems to global change.

43 Mapping forest structural diversity over large spatial scales proved challenging due to the lack of comprehensive datasets and
44 consistent data collection methodologies, hindering our ability to predict ecosystem function at large geographic scales. Whilst
45 forest structural parameters can be measured in various ways, traditional field-based measures of stand structure are generally
46 labour-intensive and have been limited to small areas (Goodbody et al., 2023). Laser scanning, or LiDAR, has been proved a
47 sound alternative for measuring tree height from 3D data measured through echoes (Coops et al., 2021). However, data from
48 airborne LiDAR have been limited in spatial and temporal coverage to specific regions (Hancock et al., 2021). Recent advances
49 in satellite remote sensing technology and computational capabilities have made it possible to measure a range of structural
50 variables at larger scales than ever before. Notably, the Global Ecosystem Dynamics Investigation (GEDI) (Dubayah et al.,
51 2020a) instrument, placed on board the International Space Station (ISS) in December 2018, collecting LiDAR samples until
52 March 2023, has revolutionized the assessment of forest structure. Recent studies have shown how structural data collected by
53 GEDI can be used in several applications ranging from biomass estimation to the monitoring of biodiversity and ecosystem
54 disturbances (Crockett et al., 2023; Hakkenberg et al., 2023; Holcomb et al., 2024). These early examples demonstrate the
55 future potential of the GEDI mission.

56

57 Whilst the availability of GEDI data and the computational capacity to handle large datasets have opened up new opportunities
58 to map structural diversity, GEDI only collects sparse measurements of vegetation structure. Although the GEDI mission has
59 recently been extended until 2030, it is expected to cover only a minimal portion of the land surface. Depending on the
60 application of interest, continuous information on structural diversity over forests may be needed. Combining GEDI with other
61 types of satellite remote sensing data within a machine learning framework may thus be necessary for the creation of structural



62 diversity data products that have continuous coverage and that extend beyond the timeframe covered by the GEDI mission.
63 Several recent studies have successfully combined GEDI data with other remote sensing data sources to predict canopy
64 structure in areas not covered by GEDI, paving the way for mapping specific structural features of vegetation regionally and
65 globally (Aragoneses et al., 2024; Lang et al., 2023; Potapov et al., 2021; Schwartz et al., 2024). Additionally, preliminary
66 efforts to assess the potential of GEDI data to capture canopy diversity over different regions have been carried out (Schneider
67 et al., 2020). However, despite these significant advances, no efforts have been made to map forest structural diversity at a
68 continental scale in Europe.

69
70 To address the lack of readily available structural diversity data, we combined a suite of structural diversity indicators
71 calculated using GEDI data with active radar and passive optical data from the Sentinel-1, Sentinel-2, and ALOS-PALSAR
72 missions. These different sources of data were then integrated using a predictive modelling framework, based on a machine
73 learning method. The resulting models were used to predict structural diversity across Europe. Although Sentinel-1, Sentinel-
74 2 and ALOS-PALSAR-2 data have been previously used for predicting canopy height and other structural components of
75 forests, their joint use for the prediction of forest structural diversity has not yet been attempted. Our analysis includes a total
76 of eight structural diversity metrics, including metrics that quantify the vertical and horizontal heterogeneity of the canopy, as
77 well as metrics that quantify the heterogeneity of forest structure among GEDI observations within a given area. The dataset
78 presented here is readily available for use as input in various environmental models and analyses.

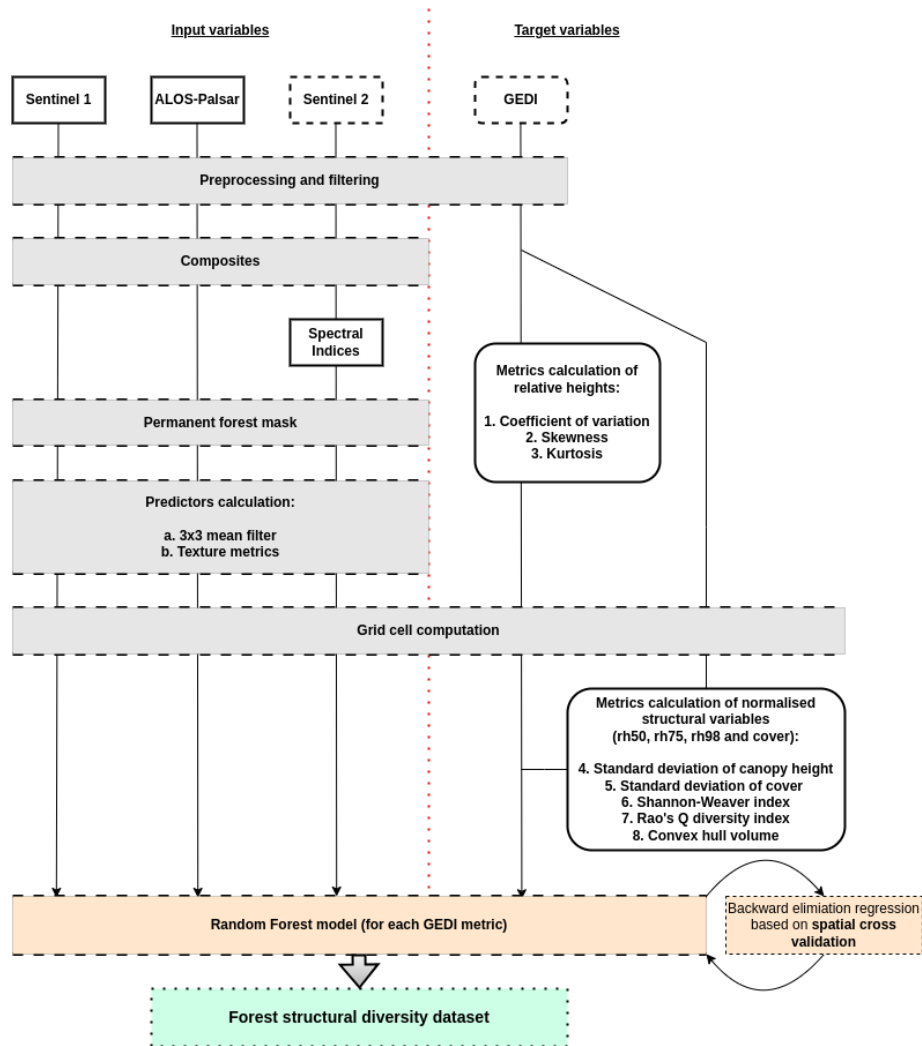
80 **2 Methods**

81
82 We calculated eight forest structural diversity metrics using NASA GEDI observations (Dubayah et al., 2020b). A list of the
83 metrics is reported in Table 1. A machine learning (ML) framework was used to model the relations between each metric and
84 a series of predictors derived from passive optical and active radar remote sensing data. The model was then used to create a
85 structural diversity dataset that covers the whole forested domain of Europe, extending up to $\sim 52^\circ$ North. The creation of the
86 dataset involved five main steps (Fig. 1): (i) satellite remote sensing data pre-processing, (ii) structural diversity metric
87 calculation (iii) model training, (iv) model validation, and (v) prediction (Fig 1). Data from GEDI, Sentinel 1 and 2, ALOS-
88 Palsar-2 were pre-processed and downloaded from Google Earth Engine (GEE), a cloud-based infrastructure that combines a
89 multi-petabyte catalogue of satellite imagery and geospatial datasets with planetary-scale analysis capabilities (Gorelick et al.,
90 2017).

91
92 We used data covering forests that had remained ecologically stable, meaning they experienced no canopy loss, from 2000 to
93 2021, as identified through the Global Forest Change product by Hansen et al. (2013). Furthermore, our analyses were limited
94 to areas where tree cover exceeded 30% and which bordered at least 6 out of 8 neighbouring pixels, also with tree cover



95 exceeding 30%. While our threshold is more stringent than Food and Agriculture Organization (FAO) definition of forest
 96 (FAO, 2000), which specifies an area spanning more than 0.5 hectares with trees taller than 5 metres and a canopy cover of
 97 more than 10%, it was chosen to capture areas with substantial arboreal density. Although our selection was guided by the
 98 FAO's broader forest criteria, we customized these guidelines to suit our research focus.



99

100 Figure 1. General workflow employed in the creation of the forest structural diversity dataset. The workflow is segmented by a red dashed
 101 line, delineating the Remote Sensing predictors from the inputs to the target GEDI data. Boxes with solid edges represent the data that were
 102 directly utilised to train the Random Forest models. Conversely, boxes with dashed edges symbolize the raw, original data from which the
 103 training data were derived. The grey boxes indicate the preliminary steps undertaken before the model training phase. The process culminates
 104 with yellow boxes, which signifies the development of the predictive model itself, leading to the green box that represents the final output
 105 outcome—the forest structural diversity dataset.

106



107 2.1 Structural diversity metrics

108 Structural diversity can be characterized in a variety of ways depending on the data from which it is calculated and the intended
109 application. In this work we adopted the common definition where diversity is defined in the vertical dimension as
110 heterogeneity of vegetation height and in the horizontal dimension as canopy heterogeneity (Hakkenberg and Goetz, 2021).
111 We chose a set of metrics that would characterize the heterogeneity within and among structural features for a given area,
112 reflecting both local (alpha) and regional (beta) measures of structural diversity. These complementary metrics have been
113 demonstrated to be particularly crucial for predicting tree diversity and ecosystem functioning (Coverdale and Davies, 2023;
114 Ma et al., 2022; Zhai et al., 2024). The metrics were also chosen to ensure they would not be redundant with structural variables
115 already provided by GEDI. A summary of the metrics with the input data used is reported in Table 1.

116

117 2.1.1 GEDI input data and general framework

118 GEDI data are collected from a full waveform LiDAR sensor operating onboard the International Space Station (ISS) from
119 April 2019 until January 2023. Due to the orbital path of the International Space Station (ISS), GEDI's coverage is primarily
120 limited to latitudes between $\sim 50^\circ$ North and south. The instrument provides sparse measurements (hereinafter sample plots or
121 shots) of vegetation structure over an area defined by a sampling footprint of about 25 m diameter.

122

123 Input data included the GEDI Level 2A Relative Heights (RH), and the Level 2B total Canopy Cover (CC) values (see Table
124 1). In the literature, rh^{98} is taken as a reference for the top canopy height (CH) (Lang 2022), CC is the proportion of the shot
125 covered by the vertical projection of the tree crowns. The GEDI data were downloaded from Google Earth Engine after
126 applying a filtering procedure (Table S1 in the Supplement).

127

128 The diversity metrics of a given area (i.e. the pixel) are calculated by collecting all the M valid GEDI shots between April
129 2019 and January 2023 overlapping the area, each shot i characterized by its RH distribution $RH_i = \{rh_i^k, rh_i^{k+1}, \dots, rh_i^{100}\}$
130 with $k: rh_i^k \geq 0$ (i.e. just the positive values were considered) and total canopy cover cc_i . Pixels with fewer observations than
131 the threshold determined by the median value were excluded, and metric values exhibiting a z-score deviation greater than 3
132 were also discarded as outliers. We conducted our calculations using three different grid resolutions: 1km, 5km and 10km.
133 These grids were set up in the Lambert Azimuthal Equal Area (LAEA) geographic projection. The largest of these grids, 10km
134 was determined to be the most suitable resolution for our study. It offers an optimal balance between accurately representing
135 forest structural features within a given area and the predictability of the structural diversity metrics derived from those
136 features. These samples were then used to compute the structural diversity metrics for that specific pixel.

137



138 In the following sections, we detail the methodology employed for calculating the diversity metrics and predictor variables,
139 which makes use of the mean $\mu(X)$, standard deviation $\sigma(X)$, skewness $\gamma(X)$, excess kurtosis $\kappa(X)$, coefficient of variation
140 $cv(X)$ of a variable $X = \{x_1, \dots, x_M\}$, where X represents a vector of observations (see Appendix A for the explicit
141 formulations).

142

143 2.1.2 Vertical Diversity Metrics

144 RH metrics provide information on the vertical distribution of the plant elements, that is, the vertical profile (VP) of the
145 vegetation (see Fig. S1 in the Supplement). The VP in a sample can be reconstructed from the corresponding RH distribution,
146 and the profile's moments (i.e. mean, standard deviation, skewness, kurtosis) are well approximated by the RH distribution's
147 moments (Fig. S1 in the Supplement).

148

149 The following calculated indicators characterise the heterogeneity of the vertical profile:

- 150 1. the average coefficient of variation of the vertical profiles

$$151 \tau_{CV} = \mu(CV)$$

152 with $CV = \{cv(RH_1), \dots, cv(RH_M)\}$. Because $cv(RH)$ shows the extent of vertical variability in relation to the expected
153 value of the VP, the latter being a measure of the central tendency, a higher τ_{CV} indicates greater dispersion and, therefore,
154 more vertical heterogeneity;

- 155 2. the average skewness of the vertical profiles

$$156 \tau_{SK} = \mu(\Gamma)$$

157 with $\Gamma = \{\gamma(RH_1), \dots, \gamma(RH_M)\}$. Skewness $\gamma(RH)$, or third standardized moment is a measure of the asymmetry of the VP
158 about its mean, and it can be positive, negative, or zero (Fig. S2 in the Supplement). If VP is an unimodal distribution (a
159 distribution with a single peak), positive skewness generally indicates an asymmetric tail extending toward larger height values
160 (overstorey heterogeneity), while negative skewness suggests a tail extending toward smaller height values (understorey
161 heterogeneity). However, note that in the cases where one tail is long, but the other tail is fat, or the distribution is multi-
162 modal, skewness does not always obey this simple rule.

163

164

- 165 3. the average excess kurtosis of the vertical profiles

$$166 \tau_{KU} = \mu(K)$$

167 with $K = \{\kappa(RH_1), \dots, \kappa(RH_M)\}$. Excess kurtosis $\kappa(RH)$ is a measure of the "tailedness" of the VP, and it is equal to 0 for
168 any univariate normal distribution, (Fig. S2 in the Supplement). Distributions with negative/positive excess kurtosis are said
169 to be platykurtic/leptokurtic. Platykurtic distributions show fewer and/or less extreme outliers than the normal distribution. In



170 this case, the vegetation mass is more concentrated around the VP mean than near the vertical extremes (i.e. the ground and to
171 top canopy height). However, it is important to note that while kurtosis, the fourth moment, does play a role in characterizing
172 the shape of VP, its influence is comparatively smaller than that of the standard deviation, the second moment, and skewness,
173 the third moment. For instance, two distinct VPs may exhibit identical excess kurtosis while displaying markedly disparate
174 distributions in terms of standard deviations.

175

176 2.1.3 Horizontal Diversity Metrics

177 We calculated 5 vertical horizontal diversity indices.

178

179 1. the standard deviation of the canopy heights

$$180 \tau_{CH} = \sigma(CH)$$

181 with $CH = \{rh_1^{98}, \dots, rh_M^{98}\}$. τ_{CH} indicates the spread of the canopy heights in the area.

182 2. the standard deviation of the total canopy cover

$$183 \tau_{CC} = \sigma(CC)$$

184 with $CC = \{cc_1, \dots, cc_M\}$. τ_{CC} indicates the spread of the total canopy cover in the area.

185

186 2.1.3 Combined Vertical and Horizontal and Diversity Metrics

187

188 3. the Shannon-Weaver index

$$189 \tau_{SW} = - \sum_{\varepsilon\pi\omega} p_{\varepsilon\pi\omega} \log p_{\varepsilon\pi\omega}$$

190 in a 4D cartesian space defined on the basis $(rh^{50}, rh^{75}, rh^{98}, cc)$, where $p_{\varepsilon\pi\omega}$ is the fraction of the GEDI samples falling
191 in a specific bin (see Appendix A2). We used a 5-unit bin size on each axis, and the GEDI CC values were amplified by 10.

192 τ_{SW} measures the uncertainty or disorder inherent to the variable's possible outcomes. $\tau_{SW} = 0$ when all observations are
193 confined within a single bin, otherwise τ_{SW} is larger than zero. Higher values indicate heterogeneity, while lower values suggest
194 homogeneity.

195 4. Rao's quadratic diversity index

$$196 \tau_{RAO} = \sum_{\varepsilon\pi\omega} \sum_{\varepsilon'\pi'o'\omega'} p_{\varepsilon\pi\omega} D_{\varepsilon\pi\omega}^{\varepsilon'\pi'o'\omega'} p_{\varepsilon'\pi'o'\omega'}$$



197 in the 4D cartesian space defined on the basis $(rh^{50}, rh^{75}, rh^{98}, cc)$, where $p_{\varepsilon\pi o\omega}$ is the fraction of the GEDI samples falling
 198 in a specific bin and $D_{\varepsilon\pi o\omega}^{\varepsilon'\pi'o'\omega'}$ the cartesian distance between two bins (see Appendix A2). We used a 1-unit bin size on each
 199 axis, and the GEDI CC values were amplified by 10. τ_{RAO} ranges from zero, indicating no diversity, to positive numbers.
 200 Differently from τ_{SW} index, τ_{RAO} considers both abundance ($p_{\varepsilon\pi o\omega}$ terms) and dissimilarity in the sampled data ($D_{\varepsilon\pi o\omega}^{\varepsilon'\pi'o'\omega'}$
 201 term).

202 5. convex hull volume

$$203 \quad \tau_{CVH} = CVH(SHT)$$

204 in the 4D cartesian space defined on the basis $(rh^{50}, rh^{75}, rh^{98}, cc)$. We used a 1-unit bin size on each axis, and the GEDI
 205 CC values were amplified by 10. CVH is the function calculating the convex hull volume on the ensemble $SHT =$
 206 $\{sht_1, \dots, sht_M\}$, with $sht_i = (rh_i^{50}, rh_i^{75}, rh_i^{98}, cc_i)$. Larger volumes indicate increased heterogeneity.

207

208 Table 1. Structural diversity metrics computed in this study.

209

Metric	Description	Units	GEDI data	Diversity
τ_{CV}	VP coefficient of variation	-	RH	vertical
τ_{SK}	VP skewness	-	RH	vertical
τ_{KU}	VP excess kurtosis	-	RH	vertical
τ_{CH}	CH standard deviation	m	rh^{98}	horizontal
τ_{CC}	CC standard deviation	-	cc	horizontal
τ_{SW}	Shannon-Weaver index	-	$(rh^{50}, rh^{75}, rh^{98}, cc)$	combined
τ_{RAO}	Rao's quadratic entropy index	-	$(rh^{50}, rh^{75}, rh^{98}, cc)$	combined
τ_{CVH}	Convex Hull volume	-	$(rh^{50}, rh^{75}, rh^{98}, cc)$	combined

210

211

212 2.2 Predictor variables

213 The variables used as ML predictors were calculated from Sentinel-1, Sentinel-2, and ALOS-Palsar-2 observed data, via the
 214 following steps:

- 215 1. appropriate bands/indices ϕ_α were calculated from the remote sensing raster images;
- 216 2. the $\phi_{\alpha,i}^\beta$ values, with β equal to SM, ASM, ENT, or DISS, are calculated from the pixels within the 7x7 window
 217 aligned with the footprint of the GEDI shot i . $\phi_{\alpha,i}^{SM}$ is the spatial mean. $\phi_{\alpha,i}^{ASM}$, $\phi_{\alpha,i}^{ENT}$, and $\phi_{\alpha,i}^{DISS}$ are the texture metrics
 218 Angular Second Moment (ASM), entropy, and dissimilarity index, respectively (see Appendix A3).



219 3. the raster images of the predictors were computed as $\phi_{\alpha}^{\beta} = \mu(\Phi_{\alpha}^{\beta})$, where the mean is calculated on the M values
220 $\Phi_{\alpha}^{\beta} = \{\phi_{\alpha,1}^{\beta}, \dots, \phi_{\alpha,M}^{\beta}\}$ corresponding to the geographical positions that overlap the image pixels.

221 In the following, we present what satellite remote sensing data were used and how they were combined for the calculation of
222 the indices. A total of 47 predictors were derived. A summary of the predictors is reported in Table S2 in the Supplement.

223 2.2.1 Sentinel-1 radar data

224 The European Space Agency's (ESA) Sentinel-1 (S1) comprises a constellation of two polar-orbiting satellites, sun-
225 synchronous orbit with a 12-day repeat cycle, which operate day and night a C-band ($\lambda = 5.5$ cm) Synthetic Aperture Radar
226 (SAR) to capture data at a spatial resolution of approximately 10 meters. The radar enables the acquirement of imagery
227 regardless of the weather, and the C-band frequency is particularly effective in interacting with fine vegetative elements such
228 as leaves and branches (Naidoo et al., 2015). In our study, from Sentinel-1 we utilized both backscatter and coherence data.

229 Backscatter is the portion of the outgoing radar signal that the target redirects directly back towards the radar antenna. The
230 backscatter characteristics provide crucial insights into the physical properties of forest canopies. For the year 2020, we focused
231 on the signal dual-polarization VV and VH Sentinel-1A (S1A) and Sentinel-1B (S1B) Ground Range Detected (GRD) data,
232 acquired in the Interferometric Wide (IW) swath mode, as it predominantly covers land masses (Kellndorfer et al., 2022).
233 VV(H) is a mode that transmits vertical waves and receives vertical (horizontal) waves to create the SAR image. We selected
234 data from the descending orbit, which has been shown to exhibit fewer correlations with evapotranspiration (ET) (Mueller et
235 al., 2022). Sentinel-1 data used in this study were obtained from Google Earth Engine, where they had already undergone some
236 pre-processing. Preprocessing steps carried out by the Google Earth Engine team include applying the orbit file for geocoding,
237 removing GRD border noise and thermal noise, and performing radiometric calibration. We performed a radiometric terrain
238 correction following (Vollrath et al., 2020), as well as the removal of stripes and edges. We selected all the valid images
239 captured over Europe within a six-month window, centred around the day of maximum NDVI from the Sentinel-2 dataset
240 (explained in section 2.2.3). We then derived:

- 241 1. the S1 backscatter six-month mean $\phi_{S1VVgs\mu}$ and $\phi_{S1VHgs\mu}$, where the mean is intended to mitigate speckle noise
242 while emphasizing the vegetation growing season;
- 243 2. the S1 backscatter standard deviation growing season $\phi_{S1VVgs\sigma}$ and $\phi_{S1VHgs\sigma}$;
- 244 3. the S1 backscatter bi-monthly mean $\phi_{S1VVpre\mu}$ and $\phi_{S1VHpre\mu}$ for a window extending two months before the month
245 before the peak, $\phi_{S1VVact\mu}$ and $\phi_{S1VHact\mu}$ for the period spanning one month before to one month after the peak, and
246 $\phi_{S1VVpost\mu}$ and $\phi_{S1VHpost\mu}$ for the two months after the month after the peak.

247 Coherence is the relationship between waves in a beam of electromagnetic (EM) radiation. Two wave trains of EM radiation
248 are coherent when they are in phase. In radar, the term coherence is also used to describe systems that preserve the phase of
249 the received signal. Coherence measurements serve as a valuable tool for monitoring temporal changes in forested



250 environments (Bruggisser et al., 2021; Cartus et al., 2022). The coherence data utilized in this study were extracted from the
251 dataset developed by Kelldorfer et al. (2022). This dataset is the product of multi-temporal, repeat-pass interferometric
252 processing of S1 SAR images. It incorporates signal dual-polarization VV and VH data from S1A and S1B in Single Look
253 Complex (SLC) format, utilizing the IW swath mode from the year 2020. The product is divided into seasonal sets, and we
254 selected summer (June-August) coherence metrics ϕ_{CO} , aligned with the growing season, employing a 12-day repeat-pass
255 interval to optimize the balance between image continuity and temporal resolution. This interval was chosen to minimize gaps
256 in the image series, compared to shorter intervals (such as 6 days), while longer intervals (e.g., 18, 24, 36, or 48 days) could
257 result in excessive decorrelation. With a relatively unchanged scene between acquisitions, higher coherence values are
258 achieved, which correlate strongly with the radar signal and hence, reduce noise levels. Furthermore, we prioritized signal VV
259 polarization to enhance our understanding of the data, as it minimizes vegetation decorrelation effects (Pan et al., 2022)

260

261 2.2.2 ALOS-PALSAR-2 radar data

262

263 The ALOS-PALSAR-2 (Advanced Land Observing Satellite - Phased Array type L-band Synthetic Aperture Radar) system,
264 developed by the Japan Aerospace Exploration Agency (JAXA), operates in the L-band frequency ($\lambda = 23.62$ cm) at a spatial
265 resolution of 25 meters. The L-band is particularly effective at penetrating canopy layers to provide backscatter signals from
266 larger vegetative features such as branches and trunks, and even from the ground. For our analysis, we made use of the global
267 mosaic of backscatter annual composites, which incorporate signal dual-polarization HH and HV data (Shimada et al., 2014)
268 from the years 2019 and 2020, accessed via GEE. In instances where the data availability was constrained for an annual
269 composite, the dataset was supplemented with observations from adjacent years. To ensure the reliability of our dataset and
270 account for possible gaps in observations, we averaged data across two years to generate $\phi_{AP2HH\mu}$ and $\phi_{AP2HV\mu}$ data. This
271 approach helps mitigate noise and stabilize the composite images.

272

273 2.2.3 Sentinel-2 optical data

274 The ESA Sentinel-2 (S2) mission comprises a constellation of two polar-orbiting satellites placed in the same sun-synchronous
275 orbit, phased at 180° to each other. Its high revisit time (10 days at the equator with one satellite, and 5 days with 2 satellites
276 at best) allows monitoring of the Earth's surface changes. The Multi-Spectral Instrument (MSI) on board the 2 platforms
277 collects the sunlight reflected from the Earth and supplies high-resolution multispectral imagery with resolutions of 10 and 20
278 meters. Data are acquired at 10 m spatial resolution for Visible (Blue, Green, Red) and Near-Infra-Red (NIR) bands, and at 20
279 m spatial resolution for VNIR-Red Edge (RE1, RE2, RE3, RE4) and Short Wave Infra-Red (SWIR) bands (SWIR1, SWIR2).
280 The Level-2A product provides atmospherically corrected Surface Reflectance (SR) images. In this study we used all the
281 Level-2A images from 2000 to 2021 identified by a scene-level cloud and snow cover smaller than 70% and 5%, respectively,
282 as provided by Google Earth Engine. We then calculated:

- 283 1. the Normalized Difference Vegetation Index



284
$$\phi_{NDVI} = \frac{\rho_{NIR} - \rho_{Red}}{\rho_{NIR} + \rho_{Red}}$$

285 as proposed by (Rouse et al., 1974) it is a widely recognized index strongly correlated with vegetation health and primary
286 productivity;

287 2. the Normalized Difference Water Index

288
$$\phi_{NDWI} = \frac{\rho_{NIR} - \rho_{SWIR1}}{\rho_{NIR} + \rho_{SWIR1}}$$

289 as proposed by (Gao, 1996), it is correlated with leaf water content.

290 3. the Normalized Difference Red Edge Index

291
$$\phi_{NDRE} = \frac{\rho_{NIR} - \rho_{RE1}}{\rho_{NIR} + \rho_{RE1}}$$

292 as proposed by Gitelson and Merzlyak, (1994) it offers sensitivity to chlorophyll content and is useful in assessing forest
293 composition and canopy cover;

294 4. the Modified Soil Adjusted Vegetation Index

295
$$\phi_{MSAVI} = \frac{2 \cdot \rho_{NIR} + 1 - \sqrt{(2 \cdot \rho_{NIR} + 1)^2 - 8 \cdot (\rho_{NIR} - \rho_{Red})}}{2}$$

296 as proposed by (Qi et al., 1994), it is suited to monitoring vegetation density and dynamics, particularly during early growth
297 stages when bare soil is prevalent, thereby minimizing soil background effects;

298 5. the Green Normalized Difference Vegetation Index

299
$$\phi_{GNDVI} = \frac{\rho_{NIR} - \rho_{Green}}{\rho_{NIR} + \rho_{Green}}$$

300 as proposed (Gitelson and Merzlyak, 1998), it responds to chlorophyll concentration and is indicative of vegetation
301 composition, structure, habitat conditions, and species diversity;

302 6. the standard deviation of NDVI

303
$$\phi_{NDVI\sigma} = \sigma(\phi_{NDVI})$$

304 as noted by (Perrone et al., 2024), it accounts for a significant portion of the variability observed in-situ plant diversity.

305

306 **2.3 Model training and validation**

307

308 We used a machine learning method - Random Forest (Breiman, 2001) - to quantify the relations between the remote sensing
309 predictors and the eight metrics. Random Forest is an ensemble learning method based on decision trees that is widely
310 employed for regression tasks. A key advantage of Random Forests is that model fitting is relatively fast and hyperparameter
311 optimization requires only a moderate amount of tuning, compared to other machine learning methods. Optimization of the
312 Random Forest model typically involves tuning a number of hyperparameters. These include the size of the forest (i.e. the



313 number of decision trees), the method of bootstrapping samples, and the setting of the maximum depth for the trees. We
314 specified a fixed number of trees, 600; bootstrapping, a technique that involves random sampling with replacement, which
315 contributes to the diversity of the decision trees in the model and helps prevent overfitting; and we did not impose any
316 limitations on the depth of the individual decision trees, allowing them to expand fully. To evaluate the performance of the
317 Random Forest model, we used mean squared error (MSE) as the metric.

318 To mitigate the potential for overfitting, we used a backward stepwise selection process that begins with a full model including
319 all available predictors. The algorithm then iteratively removes the least important feature, as determined by its contribution
320 to model performance. The relative importance of predictors was assessed using a permutation procedure (Altmann et al.,
321 2010). At each iteration, the model complexity is reduced by one predictor, and the resulting model is evaluated. We compared
322 each newly simplified model to the immediate predecessor to determine whether there was an improvement in performance or
323 a decrease that was less than 1% worse. The elimination process is halted if the removal of additional predictors causes the
324 model's performance to decrease by more than 1% compared to the previous iteration. At each step, a spatial cross-validation
325 procedure is used to assess the performance of the model. The metric we utilized to assess model performance throughout this
326 process was the coefficient of determination (R^2).

327 To validate the reduced models, we used two types of validation techniques to assess their predictive accuracy and robustness:

- 328 • Random train-validation split: in this approach, the dataset was randomly split, allocating 33% for model validation.
329 Random validation is a common method that provides a quick and often effective means of evaluating model
330 performance on unseen data. However, it has a notable drawback when dealing with spatial data: it disregards the
331 spatial structure inherent in the dataset (i.e. points close to each other are, generally, more similar than points further
332 away). By ignoring this spatial autocorrelation, random validation may inadvertently conceal overfitting issues,
333 leading to an overly optimistic perception of the model's predictive capabilities.
- 334 • 10-Fold Spatial Cross-Validation (Roberts et al., 2016): we implemented a 10-fold spatial cross-validation procedure
335 to address the shortcomings of random validation, thus reducing the overfitting. This more sophisticated method
336 partitions the data into ten spatially distinct subsets, or folds, ensuring that each fold comprises disjointed sets that are
337 geographically separated. The partitioning is achieved by clustering data points according to their spatial coordinates,
338 which preserves the spatial structure and autocorrelation present in the dataset. During the validation process, each
339 fold is used once as a validation set while the remaining folds serve as the training set. This technique provides a more
340 realistic evaluation of the model's performance and its ability to generalize across different spatial regions, thereby
341 offering a safeguard against overfitting and ensuring a more reliable assessment of the model's true predictive power.

342 Models were fitted to datasets created at different resolutions including data calculated at 10 km, 5 km and 1 km. Prediction
343 uncertainty was quantified by calculating the standard deviation of predictions across the ensembles of decision trees in the
344 Random Forest models. This metric captures the variability in predictions among individual trees within each model, providing
345 a measure of uncertainty associated with predictions for the different response variables.



346

347 3 Results

348

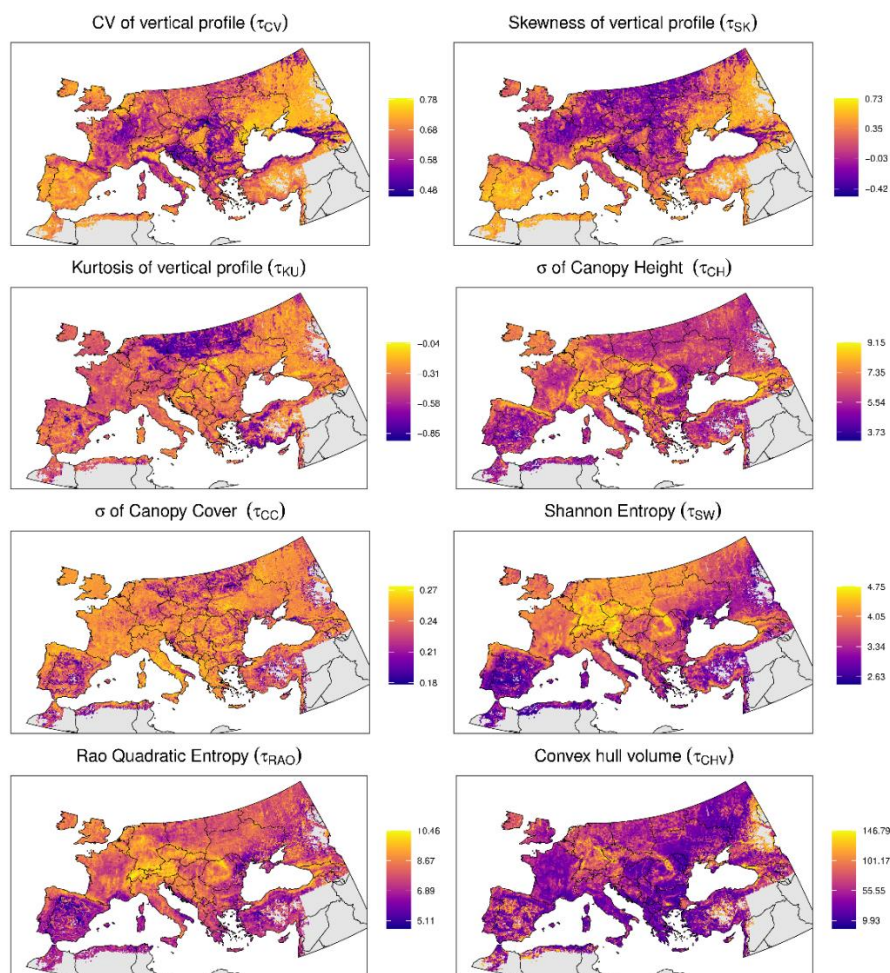
349 3.1 Predicted patterns of forest structural diversity

350 The dataset includes spatial grids for eight structural diversity metrics at three different resolutions (10 km, 5km and 1 km).

351 These metrics show a significant variation in structural diversity across the European forests as shown in Fig. 2 (see also Fig.

352 S3 and Fig. S4 in the Supplement for 5km and 1km resolution datasets).

353



354

355 Figure 2. Predicted structural diversity at a 10 km resolution, derived from the Random Forest modelling. Each panel illustrates the geographic distribution

356 of a specific metric (see methods for metric details). The colour palette transitions from purple to yellow, denote an increasing gradient of structural diversity,

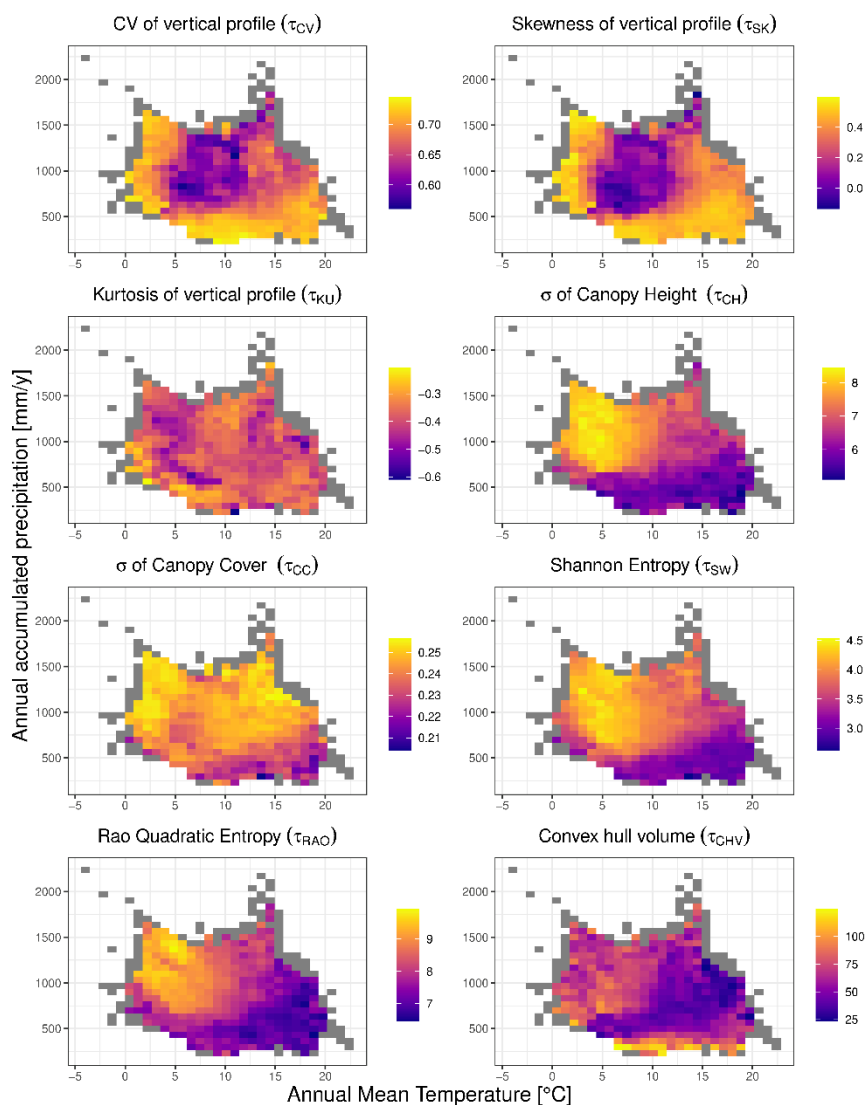
357 with warmer colours signifying higher values.

358

359



360 An examination of the variability in the 10 km resolution metrics in climate space revealed distinct patterns along temperature
361 and precipitation gradients (Fig. 3).
362



363

364 Figure 3. Predicted structural diversity variables in climate coordinates. The results refer to the dataset at 10 km resolution. Coloured bins depict variation in
365 structural diversity, calculated as the average of the structural diversity values falling within each bin. Grey bins indicate those containing fewer than 5
366 observations, for which the average was not calculated.

367

368 Patterns of variability in metrics describing vertical heterogeneity showed significant differences when comparing the
369 coefficient of variation (τ_{CV}) and skewness (τ_{SK}) against kurtosis (τ_{KU}). The coefficient of variation and skewness primarily
370 exhibited high values at the extremes of the climatic gradient. This is observed in warm and arid climates where total annual



371 precipitation is below ~500 mm and Annual Mean Temperature is above ~10 °C, as well as in colder climates where Annual
372 Mean Temperature is below ~5 °C. Patterns of variability in the kurtosis were more nuanced, consistently showing negative
373 values across the European domain, which suggests a tendency for a platykurtic distribution in the vertical profile of canopies
374 under diverse environmental conditions. The most pronounced negative kurtosis values were observed for the northern part of
375 the temperate climate zone (Fig. 3). By contrast, more heterogeneous patterns occurred in other areas such as those with a
376 Mediterranean climate, showing high variability (Fig. 3).

377 Diversity metrics describing structural heterogeneity in horizontal space, as well as combined metrics, (τ_{CH} , τ_{CC} , τ_{SW} , τ_{RAO} ,
378 τ_{CVH}) also showed considerable variability along precipitation and temperature gradients. With the exception of the convex
379 hull (τ_{CVH}), all metrics displayed low diversity values in hot and dry climates. Specifically, a combination of precipitation
380 levels below ~500 mm and annual mean temperatures above ~10°C (Fig. 3) was associated with the lowest levels of diversity.
381 By contrast, the highest levels of diversity generally occurred in areas with higher precipitation levels (> 500 mm).

382

383 Patterns of variability in the metrics in climate space for 5km and 1 km resolution (see Fig S5 and Fig S6 in the Supplement)
384 dataset were broadly concordant with the 10km dataset, indicating that the results are insensitive to the grain size at which they
385 were calculated. The metrics for the 10 km dataset generally showed low to modest amounts of intercorrelation (Fig. 4D and
386 Fig. S7 in the Supplement). This pattern was also consistent for the higher resolution datasets (5 km and 1 km) (Fig. S7, Fig.
387 S9D and Fig. S10D in the Supplement).

388

389 **3.2 Variable importance and model performance**

390 The final models, derived from the stepwise backward elimination procedure, retained between 7 and 23 predictors,
391 representing the extremes observed across various resolutions of input data and output variable types. The number of selected
392 predictors generally increased with the resolution of the input data (Fig S8 in the Supplement). Models trained for standard
393 deviation of canopy cover (τ_{CC}) and convex hull (τ_{CVH}) retained the highest number of predictors. In contrast, models for
394 skewness (τ_{SK}) and Rao quadratic entropy (τ_{RAO}) retained the lowest number of predictors (Fig S8 in the Supplement).

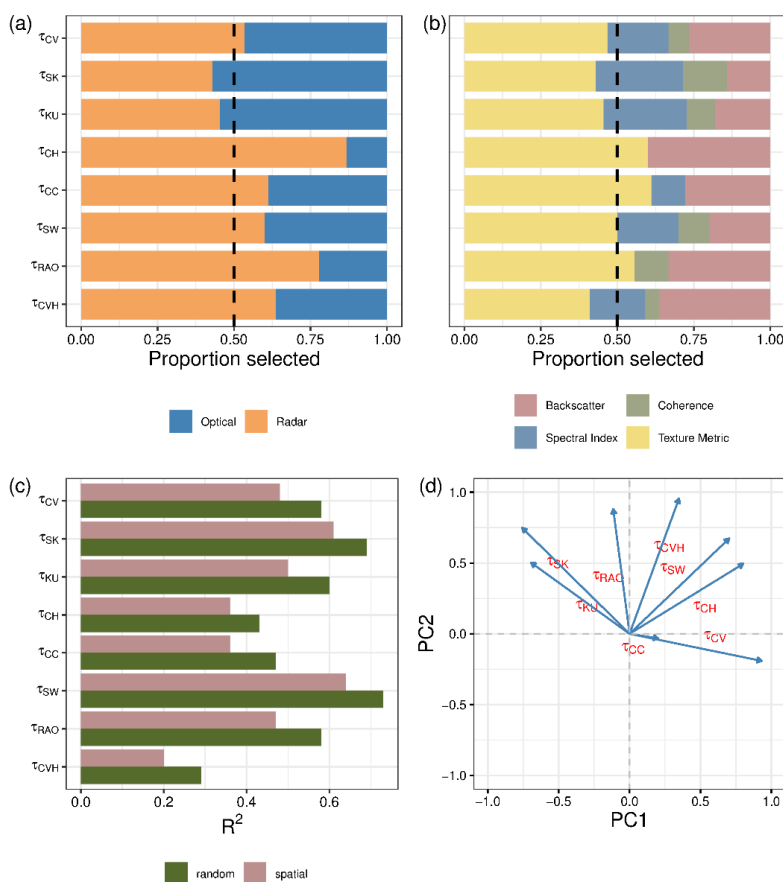
395 An examination of the type of predictors selected in the final models highlighted the importance of radar-related predictors,
396 over optical ones as shown in Fig. 4A (see Fig. S9A and Fig. S10A in the Supplement for the 5 km and 1 km datasets). The
397 average proportion of radar-related variables selected across all diversity metrics and resolutions was 0.64, although there was
398 considerable variability. In general, as the resolution of the input dataset increased, the proportion of radar-related variables
399 selected through the feature elimination procedure also increased (Fig. 4A; for the 5 km and 1km datasets see Fig. S9A and
400 Fig. S10A in the Supplement). The diversity variables for which the highest number of radar-related predictors were selected
401 was the convex hull (τ_{CVH}). On the other hand, the one for which the highest number of optical-related predictors were selected,
402 was canopy cover (τ_{CC}).

403 Among the predictors retained in the final models, texture-related types were the most commonly selected, followed by
404 backscatter, spectral indices, and coherence (Fig. 4B; for the 5 km and 1km datasets see Fig. S9B and Fig. S10B in the



405 Supplement). Notably, texture metrics constituted, on average, the largest proportion of selected variables at a 10 km resolution
 406 (Fig 4B). Conversely, the proportion of backscatter-related variables and spectral indices increased in models using the finer
 407 resolution input data (Fig. S9B and Fig. S10B in the Supplement).

408
 409



410
 411 Figure 4. Results of the random forest modelling exercise at 10 km resolution. Panels display the variable selection frequencies (A and B)
 412 and model performance, as indicated by the R^2 values derived from two types of validation methods (C). Panel D shows the results of the
 413 Principal Component Analysis (PCA) conducted on the predicted metrics at this resolution.

414
 415 Model validation revealed that random cross-validation consistently outperformed spatial cross-validation across all
 416 resolutions. The 10 km resolution analysis, the model for Shannon index τ_{SW} achieved the highest scores, with 0.73 in random
 417 validation and 0.64 in spatial validation (Fig 4C and Tables B1 and B2). Conversely, the model with convex hull (τ_{CVH}) as a
 418 variable showed the lowest performance, scoring 0.29 in random cross-validation and 0.20 in spatial cross-validation. The
 419 best-performing models at 5 km and 1 km differed from those at 10 km. These trends varied across resolutions, with skewness



420 models (τ_{SK}) yielding the best results at both 5 km and 1 km, while cover (τ_{CC}) was the worst-performing at 1 km and convex
421 hull (τ_{CVH}) at 5 km (Tables B1 and B2; Fig. S9C and Fig. S10C in the Supplement)

422

423 An examination of the standard deviation of predictions revealed generally increasing trend of prediction uncertainty across
424 resolutions (Fig. S11, Fig. S12 and Fig. S13 in the Supplement), except in Rao (τ_{RAO}) and convex hull (τ_{CVH}). Generally, low
425 standard deviations in the predictions from the models are observed across the spatial domain of interest, reflecting limited
426 variability within the ensemble. Notable exceptions occur in the Mediterranean region for the convex hull, kurtosis, and
427 standard deviation of canopy height metrics. Further variability is observed in Eastern Europe, particularly for the convex hull,
428 skewness, kurtosis, Shannon index, and standard deviation of canopy height.

429

430 **4. Discussion**

431 **4.1. Model-based predictions of structural diversity**

432

433 Our dataset provides eight metrics describing the structural heterogeneity of European forests. To our knowledge, this is the
434 first attempt to comprehensively map forest structural diversity at a quasi-continental scale (because GEDI is unable to observe
435 anything above 50° North). Datasets such as the one presented here contribute to an emerging landscape of data products based
436 on spaceborne LiDAR data, ranging from regional to global scales (e.g. Lang et al., 2023; Shendryk, 2022; Sothe et al., 2022).
437 However, while most efforts have primarily focused on mapping top canopy height, we aimed to create a set of complementary
438 metrics describing the diversity of canopy structure, an ecologically important yet neglected aspect in research.

439

440 Some of the ecological indices employed in this study are routinely applied to optical data to quantify landscape-level
441 heterogeneity using multispectral data (Tuanmu and Jetz, 2015). For instance, the Rao and Shannon diversity indices, which
442 can be calculated from spectral indices, have been widely used to quantify the heterogeneity of vegetation and are often
443 proposed as indicators of ecosystem heterogeneity (Rocchini et al., 2021). These heterogeneity indicators have proved to be
444 useful in a variety of contexts, including biodiversity modelling and quantifying the vulnerability of forest ecosystems to
445 disturbances (Forzieri et al., 2021; Taddeo et al., 2021). However, indices based solely on optical data fail to capture crucial
446 aspects of structural heterogeneity, which are related to the three-dimensional arrangement of vegetative elements in the canopy
447 (Fassnacht et al., 2022). Our study addresses a critical gap by introducing the first consistent dataset that maps structural
448 diversity across the forested domain in Europe. This development will contribute to a more detailed and robust regional analysis
449 on ecosystem dynamics, which critically depend on vegetation structure (Migliavacca et al., 2021) and structural diversity
450 (LaRue et al., 2023), and other facets of biodiversity, which requires information on the vertical profile of plants (Fassnacht et
451 al., 2022).

452



453 Our findings revealed that model performance differed according to the spatial resolutions and diversity metrics, with several
454 models achieving R^2 values indicative of moderate to strong predictive accuracy, particularly at coarser spatial resolutions
455 (Appendix B, Tables B1 and B2). This variation highlights the critical role of resolution in model performance, indicating that,
456 depending on the application of interest, coarser resolutions may optimize the utility of the models. As expected, spatial cross-
457 validation consistently yielded lower R^2 values than random train-validation random validation across most metrics and
458 resolutions. This outcome reflects the challenges inherent on machine learning methods (Meyer and Pebesma, 2021) of
459 predicting outcomes in areas geographically distinct from the training data. Nevertheless, the decrease was generally modest,
460 affirming the broad applicability of our models beyond the training domain.

461

462 The recursive feature elimination procedure highlighted the importance of textural variables (Fig. S8 in the Supplement) across
463 diversity metrics and spatial resolutions. Entropy, derived from ALOS-PALSAR-2 data, stood out as the most influential
464 variable, corroborating research that demonstrates textural metrics' effectiveness in capturing spatial heterogeneity in structural
465 diversity (Bae et al., 2019). Additionally, the significant role of coherence, which aligns with evidence of its predictive power
466 for forest structural features (Bruggisser et al., 2021; Cartus et al., 2022), suggests its potential in reflecting changes in forest
467 structural density and composition. Collectively, our findings underscore the benefits of integrating various sensor data to
468 enhance the prediction of structural diversity, as evidenced by the diverse contributions of optical and radar-based predictors.

469

470 **4.2. Potential applications**

471

472 We envisage that our structural diversity dataset will significantly advance future research and practical applications across
473 several disciplines. We identify three key areas where the dataset could be utilised.

474

475 Firstly, the dataset could aid in the development of different biodiversity indicators. Ecosystem structure has been identified
476 as an Essential Biodiversity Variable (EBV) (Valbuena et al., 2020), and a wide range of studies have shown a strong
477 correlation between LiDAR-based metrics and ground-based biodiversity measurements (Marselis et al., 2020). The metrics
478 developed here could be used to identify areas with unique structural features that harbour high levels of biodiversity.
479 Furthermore, integrating them with data from other sensors, such as Sentinel 1 and Sentinel 2, offers a promising avenue for
480 generating accurate spatial predictions of different indicators, thus paving the way for the development of frameworks for
481 monitoring long-term biodiversity changes.

482

483 Secondly, the dataset offers a valuable resource for quantifying the observed impacts of global change drivers on the
484 functioning of European forest ecosystems. The increasing recognition of the role of structural diversity in driving ecosystem
485 processes (Ali et al., 2016; Aponte et al., 2020; Listopad et al., 2015) underscores the importance of our metrics. Consequently,
486 our dataset provides a crucial tool for enabling comprehensive, data-driven assessments of the impact of climate and land cover



487 changes on the functioning of forest ecosystems across large scales, addressing the previous limitations posed by the
488 unavailability of structural diversity data over extensive spatial scales.

489

490 Thirdly, the dataset could be used for improving Earth system models. Historically, plant canopy structure has not been
491 adequately represented in these models (Atkins et al., 2018; Schneider et al., 2020). This lack of detailed representation can
492 lead to significant errors in predicting energy balance, carbon cycling, and ecosystem responses to environmental changes
493 (Duveiller et al., 2023). Integrating structural diversity into these models has the potential to enhance the accuracy of
494 simulations by incorporating more realistic representations of light interception, photosynthetic rates, and energy fluxes.

495

496 **5. Data availability**

497 The structural diversity metrics generated in this study can be accessed at Figshare:
498 <https://doi.org/10.6084/m9.figshare.26058868> (Girardello et al., 2024). All maps are available at three spatial resolutions (1
499 km, 5 km, and 10 km) in the EPSG:3035 (LAEA) spatial reference system.

500

501

502 . All maps are available at three spatial resolutions (1 km, 5 km, and 10 km) in the EPSG:3035 (LAEA) spatial reference
503 system.

504

505 **6. Code availability**

506 Google Earth Engine code for data preparation and data for reproducing the figures are available at
507 <https://github.com/drmarcogir/structuraldiversity>

508

509 **7. Conclusions**

510

511 We generated a spatially-explicit dataset on eight forest structural diversity metrics at multiple resolutions (10km, 5km, 1km)
512 encompassing temperate, Mediterranean, and continental regions of Europe. Models developed to create the dataset were
513 robust. The dataset generated in our study represents a novel contribution to the Essential Biodiversity Variables (EBV)
514 framework, and the metrics can be used in various applications, ranging from the study of biodiversity to ecosystem
515 functioning. We conclude that combining GEDI data with those from other satellite sensors paves the way for developing a
516 consistent and scalable framework to monitor structural diversity across Europe.

517

518

519

520



521

522

523 **Appendices**

524

525 **Appendix A: Supplementary Methods**

526

527 **A1 Statistical indicators**

528 The statistical indicators used in this study are detailed below. The mean μ , standard deviation σ , skewness γ , excess kurtosis
 529 κ , coefficient of variation cv of a variable $X = \{x_1, \dots, x_N\}$ are defined as:

530

531

$$\mu(X) = \frac{1}{N} \sum_{i=1}^N x_i$$

532

$$\sigma(X) = \left\{ \frac{1}{N} \sum_{i=1}^N [x_i - \mu(X)]^2 \right\}^{1/2}$$

533

$$\gamma(X) = \frac{\sum_{i=1}^N [x_i - \mu(X)]^3}{[\sigma(X)]^3}$$

534

$$\kappa(X) = \frac{\sum_{i=1}^N [x_i - \mu(X)]^4}{[\sigma(X)]^4}$$

534

536

$$cv(X) = \frac{\sigma(X)}{\mu(X)} \quad (A1)$$

537

538 **A2 Binning in cartesian 4d space**

539

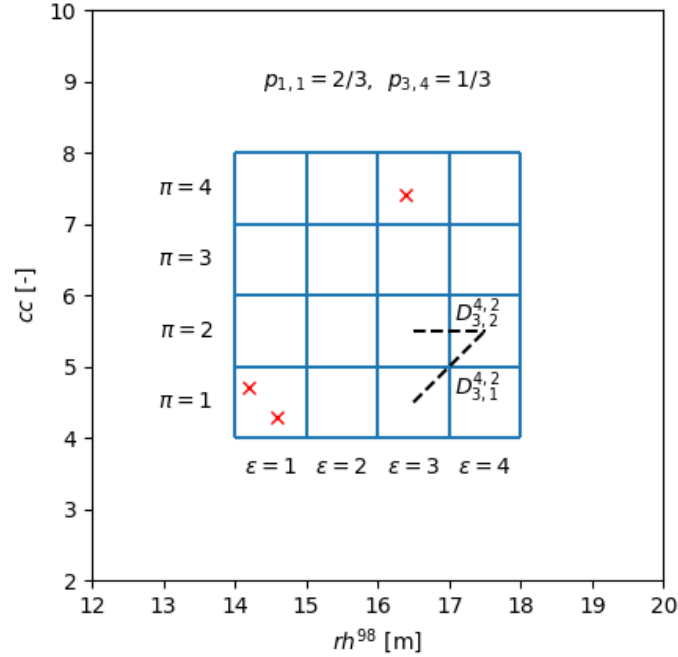
540 $p_{\varepsilon\pi o\omega}$ indicates the fraction of the GEDI shots falling in the bin identified by the indices $(\varepsilon, \pi, o, \omega)$ in the 4D cartesian space
 541 defined on the basis $(e^\varepsilon, e^\pi, e^o, e^\omega)$, see Figure S2, with

542

$$\sum_{\varepsilon\pi o\omega} p_{\varepsilon\pi o\omega} = 1 \quad (A2)$$

543 where $\sum_{\varepsilon\pi o\omega}$ stands for $\sum_{\varepsilon=1}^{N_{bins}^\varepsilon} \sum_{\pi=1}^{N_{bins}^\pi} \sum_{o=1}^{N_{bins}^o} \sum_{\omega=1}^{N_{bins}^\omega}$, with N_{bins}^ε number of bins in the e^ε dimension, and $D_{\varepsilon\pi o\omega}^{\varepsilon'\pi'o'\omega'}$
 544 indicates the cartesian distance between $(\varepsilon, \pi, o, \omega)$ and $(\varepsilon', \pi', o', \omega')$ bin.

545



546

547 Figure A1. example of $p_{\epsilon\pi}$ and $D_{\epsilon\pi}^{\epsilon'\pi'}$ estimation in the 2D cartesian space defined on the basis (rh^{98}, cc) . The GEDI shots are
 548 reported with the red X, GEDI cc values have been amplified by 10.

549

550 A3 Predictor calculation

551 Starting with appropriate bands/indices (step 2 of the workflow in the main text), the four scalars $\phi_{\alpha,i}^{\beta}$, where $\beta \in$
 552 $\{SM, ASM, ENT, DISS\}$, are calculated from the cluster of 7×7 pixels $\phi_{\alpha,i}(p, q)$ overlapping the footprint of the GEDI shot
 553 i , where p and q represent the pixel indices within the window. In details, we calculated:

- 554 1. the spatial mean (SM)

555

$$\phi_{\alpha,i}^{SM} = \mu(\phi_{\alpha,i}(p, q)) \quad (A3)$$

556 which is performed to compensate for potential footprint geolocation inaccuracies, and reduce the presence of noise, and three
 557 texture metrics. Texture metrics provide spatial content information (Nichol and Sarker 2011), and are highly effective in
 558 capturing the pixels heterogeneity. Defining $\bar{\phi}_{\alpha,i}(p, q)$ as the grey-levels matrix, which is calculated from $\phi_{\alpha,i}(p, q)$ by
 559 normalizing the values* within the range of $[0, 1]$ based on the 1st and 99th percentiles, $C_{\alpha,i}(m, n)$ as the corresponding grey-
 560 levels co-occurrence matrix (GLCM), with dimension 256×256 (Haralick et al. 1973):

$$561 \quad C_{\alpha,i}(m, n) = \sum_{p=1}^7 \sum_{q=1}^6 1, \text{ if } \bar{\phi}_{\alpha,i}(p, q) = m \text{ and } \bar{\phi}_{\alpha,i}(p, q+1) = n; 0, \text{ otherwise}$$



562 and $p_{\alpha,i}(m, n)$ as the probability that grey-level m occurs close to the grey-level n :

563
$$p_{\alpha,i}(m, n) = \frac{c_{\alpha,i}(m,n)}{\sum_{p=0}^{255} \sum_{q=0}^{255} c_{\alpha,i}(p,q)} \quad (\text{A4})$$

564 we calculated:

565

566 2. the angular second moment (ASM)

567
$$\phi_{\alpha,i}^{ASM} = - \sum_{m=0}^{255} \sum_{n=0}^{255} [p_{\alpha,i}(m, n)]^2 \quad (\text{A5})$$

568 ASM is a measure of the homogeneity or uniformity of pixel values within a neighbourhood. It reflects the degree to which
569 pixel values deviate from the mean, providing insights into the texture's smoothness or roughness;

570 3. the entropy

571
$$\phi_{\alpha,i}^{ENT} = - \sum_{m=0}^{255} \sum_{n=0}^{255} p_{\alpha,i}(m, n) \log p_{\alpha,i}(m, n) \quad (\text{A6})$$

572 Entropy is a measure of the randomness or disorder in the distribution of grey levels. It quantifies image non-uniformity, with
573 higher entropy values indicating a more random distribution of pixel values within a neighbourhood;

574 4. the dissimilarity index

575
$$\phi_{\alpha,i}^{DISS} = \sum_{m=0}^{255} \sum_{n=0}^{255} p_{\alpha,i}(m, n) |m - n| \log p_{\alpha,i}(m, n) \quad (\text{A7})$$

576 Dissimilarity measures the complexity and the nature of grey-level transitions among neighbouring pixels (Connors et al.
577 1984). It quantifies image contrast, with higher dissimilarity values reflecting pronounced differences among neighbouring
578 pixel values.

579 * For Sentinel-2 data, we retained only pixels with NDVI values greater than 0, as values below 0 are more likely to represent
580 non-vegetative features.

581

582

583

584

585

586

587

588

589

590

591

592

593



594 **Appendix B: Model validation results**

595

596 Table B1. Results of the random validation procedure conducted for the forest structural metrics at three spatial resolutions:
 597 1x1km, 5x5km, and 10x10km. The validation outcomes are presented in terms of the coefficient of determination (R^2), which
 598 quantifies the proportion of the variance in the dependent variable that is predictable from the independent variables.

599

Metric	1 km	5 km	10 km
CV of vertical profile (τ_{CV})	0.36	0.51	0.58
Skewness of vertical profile (τ_{SK})	0.47	0.64	0.69
Kurtosis of vertical profile (τ_{KU})	0.28	0.48	0.6
σ of Canopy Height (τ_{CH})	0.26	0.39	0.43
σ of Canopy Cover (τ_{CC})	0.16	0.37	0.47
Shannon Entropy (τ_{SW})	0.39	0.63	0.73
Rao Quadratic Entropy (τ_{RAO})	0.32	0.52	0.58
Convex Hull Volume (τ_{CHV})	0.26	0.34	0.29

600

601 Table B2. Results of the spatial cross-validation procedures conducted for the forest structural metrics at three spatial
 602 resolutions: 1x1km, 5x5km, and 10x10km. The validation outcomes are presented in terms of the coefficient of determination
 603 (R^2).

604

Metric	1 km	5 km	10 km
CV of vertical profile (τ_{CV})	0.33	0.43	0.48
Skewness of vertical profile (τ_{SK})	0.43	0.57	0.61
Kurtosis of vertical profile (τ_{KU})	0.24	0.41	0.5
σ of Canopy Height (τ_{CH})	0.25	0.34	0.36
σ of Canopy Cover (τ_{CC})	0.14	0.29	0.36
Shannon Entropy (τ_{SW})	0.36	0.55	0.64
Rao Quadratic Entropy (τ_{RAO})	0.29	0.44	0.47
Convex Hull Volume (τ_{CHV})	0.2	0.25	0.2

605



606 **Author contribution** MGir, GO and AC conceived the ideas with contributions from MM, GC, and MPicc. MGar, MPick,
607 and AE contributed to the discussion on metric development and interpretation. MGir, GO, and MPicc collated and analysed
608 the data. MGir led the writing with inputs from MPicc and GO. All authors contributed to the revision of the manuscript and
609 approved the final version.

610

611 **Competing interests** The authors declare no competing financial interests

612

613 **Acknowledgements** The study was funded by the Exploratory Project ForBioRes of the European Commission, Joint Research
614 Centre

615

616

617

618

619

620

621

622

623

624

625

626

627

628

629

630

631

632

633

634

635

636

637

638

639



640 References

- 641 Ali, A., Yan, E.-R., Chen, H. Y. H., Chang, S. X., Zhao, Y.-T., Yang, X.-D., and Xu, M.-S.: Stand structural diversity rather
642 than species diversity enhances aboveground carbon storage in secondary subtropical forests in Eastern China, *Biogeosciences*,
643 13, 4627–4635, <https://doi.org/10.5194/bg-13-4627-2016>, 2016.
- 644 Altmann, A., Tološi, L., Sander, O., and Lengauer, T.: Permutation importance: a corrected feature importance measure,
645 *Bioinformatics*, 26, 1340–1347, <https://doi.org/10.1093/bioinformatics/btq134>, 2010.
- 646 Aponte, C., Kasel, S., Nitschke, C. R., Tanase, M. A., Vickers, H., Parker, L., Fedrigo, M., Kohout, M., Ruiz-Benito, P.,
647 Zavala, M. A., and Bennett, L. T.: Structural diversity underpins carbon storage in Australian temperate forests, *Global Ecology*
648 *and Biogeography*, 29, 789–802, <https://doi.org/10.1111/geb.13038>, 2020.
- 649 Aragoneses, E., García, M., Ruiz-Benito, P., and Chuvieco, E.: Mapping forest canopy fuel parameters at European scale using
650 spaceborne LiDAR and satellite data, *Remote Sens Environ*, 303, 114005, <https://doi.org/10.1016/j.rse.2024.114005>, 2024.
- 651 Atkins, J. W., Fahey, R. T., Hardiman, B. S., and Gough, C. M.: Forest Canopy Structural Complexity and Light Absorption
652 Relationships at the Subcontinental Scale, *J Geophys Res Biogeosci*, 123, 1387–1405, <https://doi.org/10.1002/2017JG004256>,
653 2018.
- 654 Bae, S., Levick, S. R., Heidrich, L., Magdon, P., Leutner, B. F., Wöllauer, S., Serebryanyk, A., Nauss, T., Krzystek, P.,
655 Gossner, M. M., Schall, P., Heibl, C., Bässler, C., Doerfler, I., Schulze, E.-D., Krah, F.-S., Culmsee, H., Jung, K., Heurich,
656 M., Fischer, M., Seibold, S., Thorn, S., Gerlach, T., Hothorn, T., Weisser, W. W., and Müller, J.: Radar vision in the mapping
657 of forest biodiversity from space, *Nat Commun*, 10, 4757, <https://doi.org/10.1038/s41467-019-12737-x>, 2019.
- 658 Breiman, L.: Random forests, *Mach Learn*, 45, 5–32, 2001.
- 659 Bruggisser, M., Dorigo, W., Dostálová, A., Hollaus, M., Navacchi, C., Schläffer, S., and Pfeifer, N.: Potential of Sentinel-1 C-
660 Band Time Series to Derive Structural Parameters of Temperate Deciduous Forests, *Remote Sens (Basel)*, 13, 798,
661 <https://doi.org/10.3390/rs13040798>, 2021.
- 662 Cartus, O., Santoro, M., Wegmuller, U., Labriere, N., and Chave, J.: Sentinel-1 Coherence for Mapping Above-Ground
663 Biomass in Semiarid Forest Areas, *IEEE Geoscience and Remote Sensing Letters*, 19, 1–5,
664 <https://doi.org/10.1109/LGRS.2021.3071949>, 2022.
- 665 Coops, N. C., Tompalski, P., Goodbody, T. R. H., Queinnec, M., Luther, J. E., Bolton, D. K., White, J. C., Wulder, M. A., van
666 Lier, O. R., and Herмосilla, T.: Modelling lidar-derived estimates of forest attributes over space and time: A review of
667 approaches and future trends, *Remote Sens Environ*, 260, 112477, <https://doi.org/10.1016/j.rse.2021.112477>, 2021.
- 668 Coverdale, T. C. and Davies, A. B.: Unravelling the relationship between plant diversity and vegetation structural complexity:
669 A review and theoretical framework, *Journal of Ecology*, 111, 1378–1395, <https://doi.org/10.1111/1365-2745.14068>, 2023.
- 670 Crockett, E. T. H., Atkins, J. W., Guo, Q., Sun, G., Potter, K. M., Ollinger, S., Silva, C. A., Tang, H., Woodall, C. W.,
671 Holgerson, J., and Xiao, J.: Structural and species diversity explain aboveground carbon storage in forests across the United
672 States: Evidence from GEDI and forest inventory data, *Remote Sens Environ*, 295, 113703,
673 <https://doi.org/10.1016/j.rse.2023.113703>, 2023.



- 674 Dubayah, R., Blair, J. B., Goetz, S., Fatoyinbo, L., Hansen, M., Healey, S., Hofton, M., Hurtt, G., Kellner, J., Luthcke, S.,
675 Armston, J., Tang, H., Duncanson, L., Hancock, S., Jantz, P., Marselis, S., Patterson, P. L., Qi, W., and Silva, C.: The Global
676 Ecosystem Dynamics Investigation: High-resolution laser ranging of the Earth's forests and topography, *Science of Remote*
677 *Sensing*, 1, 100002, <https://doi.org/10.1016/j.srs.2020.100002>, 2020a.
- 678 Dubayah, R., Blair, J. B., Goetz, S., Fatoyinbo, L., Hansen, M., Healey, S., Hofton, M., Hurtt, G., Kellner, J., Luthcke, S., and
679 others: The Global Ecosystem Dynamics Investigation: High-resolution laser ranging of the Earth's forests and topography,
680 *Science of Remote Sensing*, 1, 100002, 2020b.
- 681 Duveiller, G., Pickering, M., Muñoz-Sabater, J., Caporaso, L., Boussetta, S., Balsamo, G., and Cescatti, A.: Getting the leaves
682 right matters for estimating temperature extremes, *Geosci Model Dev*, 16, 7357–7373, [https://doi.org/10.5194/gmd-16-7357-](https://doi.org/10.5194/gmd-16-7357-2023)
683 2023, 2023.
- 684 Ehbrecht, M., Seidel, D., Annighöfer, P., Kreft, H., Köhler, M., Zemp, D. C., Puettmann, K., Nilus, R., Babweteera, F., Willim,
685 K., Stiers, M., Soto, D., Boehmer, H. J., Fisichelli, N., Burnett, M., Juday, G., Stephens, S. L., and Ammer, C.: Global patterns
686 and climatic controls of forest structural complexity, *Nat Commun*, 12, 519, <https://doi.org/10.1038/s41467-020-20767-z>,
687 2021.
- 688 FAO: On definitions of forest and forest change, 2000.
- 689 Fassnacht, F. E., Müllerová, J., Conti, L., Malavasi, M., and Schmidlein, S.: About the link between biodiversity and spectral
690 variation, *Appl Veg Sci*, 25, <https://doi.org/10.1111/avsc.12643>, 2022.
- 691 Forzieri, G., Girardello, M., Ceccherini, G., Spinoni, J., Feyen, L., Hartmann, H., Beck, P. S. A., Camps-Valls, G., Chirici, G.,
692 Mauri, A., and Cescatti, A.: Emergent vulnerability to climate-driven disturbances in European forests, *Nat Commun*, 12,
693 1081, <https://doi.org/10.1038/s41467-021-21399-7>, 2021.
- 694 Gao, B.: NDWI—A normalized difference water index for remote sensing of vegetation liquid water from space, *Remote Sens*
695 *Environ*, 58, 257–266, [https://doi.org/10.1016/S0034-4257\(96\)00067-3](https://doi.org/10.1016/S0034-4257(96)00067-3), 1996.
- 696 Girardello, M., Oton, G., Piccardo, M., and Ceccherini, G.: A dataset on the structural diversity of European forests,
697 <https://doi.org/10.6084/m9.figshare.26058868.v1>, 2024.
- 698 Gitelson, A. and Merzlyak, M. N.: Quantitative estimation of chlorophyll-a using reflectance spectra: Experiments with autumn
699 chestnut and maple leaves, *J Photochem Photobiol B*, 22, 247–252, [https://doi.org/10.1016/1011-1344\(93\)06963-4](https://doi.org/10.1016/1011-1344(93)06963-4), 1994.
- 700 Gitelson, A. A. and Merzlyak, M. N.: Remote sensing of chlorophyll concentration in higher plant leaves, *Advances in Space*
701 *Research*, 22, 689–692, [https://doi.org/10.1016/S0273-1177\(97\)01133-2](https://doi.org/10.1016/S0273-1177(97)01133-2), 1998.
- 702 Goodbody, T. R. H., Coops, N. C., Queinnec, M., White, J. C., Tompalski, P., Hudak, A. T., Auty, D., Valbuena, R., LeBoeuf,
703 A., Sinclair, I., McCartney, G., Prieur, J.-F., and Woods, M. E.: sgsR: a structurally guided sampling toolbox for LiDAR-
704 based forest inventories, *Forestry*, 96, 411–424, <https://doi.org/10.1093/forestry/cpac055>, 2023.
- 705 Gorelick, N., Hancher, M., Dixon, M., Ilyushchenko, S., Thau, D., and Moore, R.: Google Earth Engine: Planetary-scale
706 geospatial analysis for everyone, *Remote Sens Environ*, 202, <https://doi.org/10.1016/j.rse.2017.06.031>, 2017.



- 707 Gough, C. M., Atkins, J. W., Fahey, R. T., and Hardiman, B. S.: High rates of primary production in structurally complex
708 forests, *Ecology*, 100, <https://doi.org/10.1002/ecy.2864>, 2019.
- 709 Hakkenberg, C. R. and Goetz, S. J.: Climate mediates the relationship between plant biodiversity and forest structure across
710 the United States, *Global Ecology and Biogeography*, 30, 2245–2258, <https://doi.org/10.1111/geb.13380>, 2021.
- 711 Hakkenberg, C. R., Atkins, J. W., Brodie, J. F., Burns, P., Cushman, S., Jantz, P., Kaszta, Z., Quinn, C. A., Rose, M. D., and
712 Goetz, S. J.: Inferring alpha, beta, and gamma plant diversity across biomes with GEDI spaceborne lidar, *Environmental
713 Research: Ecology*, 2, 035005, <https://doi.org/10.1088/2752-664X/acffcd>, 2023.
- 714 Hancock, S., McGrath, C., Lowe, C., Davenport, I., and Woodhouse, I.: Requirements for a global lidar system: spaceborne
715 lidar with wall-to-wall coverage, *R Soc Open Sci*, 8, <https://doi.org/10.1098/rsos.211166>, 2021.
- 716 Hansen, M. C., Potapov, P. V., Moore, R., Hancher, M., Turubanova, S. A., Tyukavina, A., Thau, D., Stehman, S. V., Goetz,
717 S. J., Loveland, T. R., Kommareddy, A., Egorov, A., Chini, L., Justice, C. O., and Townshend, J. R. G.: High-Resolution
718 Global Maps of 21st-Century Forest Cover Change, *Science (1979)*, 342, 850–853, <https://doi.org/10.1126/science.1244693>,
719 2013.
- 720 Holcomb, A., Burns, P., Keshav, S., and Coomes, D. A.: Repeat GEDI footprints measure the effects of tropical forest
721 disturbances, *Remote Sens Environ*, 308, 114174, <https://doi.org/10.1016/j.rse.2024.114174>, 2024.
- 722 Kellndorfer, J., Cartus, O., Lavalle, M., Magnard, C., Milillo, P., Oveisgharan, S., Osmanoglu, B., Rosen, P. A., and
723 Wegmüller, U.: Global seasonal Sentinel-1 interferometric coherence and backscatter data set, *Sci Data*, 9, 73,
724 <https://doi.org/10.1038/s41597-022-01189-6>, 2022.
- 725 Lang, N., Jetz, W., Schindler, K., and Wegner, J. D.: A high-resolution canopy height model of the Earth, *Nat Ecol Evol*, 7,
726 1778–1789, <https://doi.org/10.1038/s41559-023-02206-6>, 2023.
- 727 Larue, E. A., Hardiman, B. S., Elliott, J. M., and Fei, S.: Structural diversity as a predictor of ecosystem function,
728 *Environmental Research Letters*, 14, <https://doi.org/10.1088/1748-9326/ab49bb>, 2019.
- 729 LaRue, E. A., Hardiman, B. S., Elliott, J. M., and Fei, S.: Structural diversity as a predictor of ecosystem function,
730 *Environmental Research Letters*, 14, 114011, <https://doi.org/10.1088/1748-9326/ab49bb>, 2019.
- 731 LaRue, E. A., Knott, J. A., Domke, G. M., Chen, H. Y., Guo, Q., Hisano, M., Oswald, C., Oswald, S., Kong, N., Potter, K. M.,
732 and Fei, S.: Structural diversity as a reliable and novel predictor for ecosystem productivity, *Front Ecol Environ*, 21, 33–39,
733 <https://doi.org/10.1002/fee.2586>, 2023.
- 734 Listopad, C. M. C. S., Masters, R. E., Drake, J., Weishampel, J., and Branquinho, C.: Structural diversity indices based on
735 airborne LiDAR as ecological indicators for managing highly dynamic landscapes, *Ecol Indic*, 57, 268–279,
736 <https://doi.org/10.1016/j.ecolind.2015.04.017>, 2015.
- 737 Ma, Q., Su, Y., Hu, T., Jiang, L., Mi, X., Lin, L., Cao, M., Wang, X., Lin, F., Wang, B., Sun, Z., Wu, J., Ma, K., and Guo, Q.:
738 The coordinated impact of forest internal structural complexity and tree species diversity on forest productivity across forest
739 biomes, *Fundamental Research*, <https://doi.org/10.1016/j.fmre.2022.10.005>, 2022.



- 740 Marselis, S. M., Abernethy, K., Alonso, A., Armston, J., Baker, T. R., Bastin, J., Bogaert, J., Boyd, D. S., Boeckx, P., Burslem,
741 D. F. R. P., Chazdon, R., Clark, D. B., Coomes, D., Duncanson, L., Hancock, S., Hill, R., Hopkinson, C., Kearsley, E., Kellner,
742 J. R., Kenfack, D., Labrière, N., Lewis, S. L., Minor, D., Memiaghe, H., Monteagudo, A., Nilus, R., O'Brien, M., Phillips, O.
743 L., Poulsen, J., Tang, H., Verbeeck, H., and Dubayah, R.: Evaluating the potential of full-waveform lidar for mapping pan-
744 tropical tree species richness, *Global Ecology and Biogeography*, 29, 1799–1816, <https://doi.org/10.1111/geb.13158>, 2020.
- 745 Meyer, H. and Pebesma, E.: Predicting into unknown space? Estimating the area of applicability of spatial prediction models,
746 *Methods Ecol Evol*, 12, 1620–1633, <https://doi.org/10.1111/2041-210X.13650>, 2021.
- 747 Migliavacca, M., Musavi, T., Mahecha, M. D., Nelson, J. A., Knauer, J., Baldocchi, D. D., Perez-Priego, O., Christiansen, R.,
748 Peters, J., Anderson, K., Bahn, M., Black, T. A., Blanken, P. D., Bonal, D., Buchmann, N., Caldararu, S., Carrara, A.,
749 Carvalhais, N., Cescatti, A., Chen, J., Cleverly, J., Cremonese, E., Desai, A. R., El-Madany, T. S., Farella, M. M., Fernández-
750 Martínez, M., Filippa, G., Forkel, M., Galvagno, M., Gomasasca, U., Gough, C. M., Göckede, M., Ibrom, A., Ikawa, H.,
751 Janssens, I. A., Jung, M., Kattge, J., Keenan, T. F., Knohl, A., Kobayashi, H., Kraemer, G., Law, B. E., Liddell, M. J., Ma, X.,
752 Mammarella, I., Martini, D., Macfarlane, C., Matteucci, G., Montagnani, L., Pabon-Moreno, D. E., Panigada, C., Papale, D.,
753 Pendall, E., Penuelas, J., Phillips, R. P., Reich, P. B., Rossini, M., Rotenberg, E., Scott, R. L., Stahl, C., Weber, U., Wohlfahrt,
754 G., Wolf, S., Wright, I. J., Yakir, D., Zaehle, S., and Reichstein, M.: The three major axes of terrestrial ecosystem function,
755 *Nature*, 598, 468–472, <https://doi.org/10.1038/s41586-021-03939-9>, 2021.
- 756 Mueller, M. M., Dubois, C., Jagdhuber, T., Hellwig, F. M., Pathe, C., Schmullius, C., and Steele-Dunne, S.: Sentinel-1
757 Backscatter Time Series for Characterization of Evapotranspiration Dynamics over Temperate Coniferous Forests, *Remote
758 Sens (Basel)*, 14, 6384, <https://doi.org/10.3390/rs14246384>, 2022.
- 759 Murphy, B. A., May, J. A., Butterworth, B. J., Andresen, C. G., and Desai, A. R.: Unraveling Forest Complexity: Resource
760 Use Efficiency, Disturbance, and the Structure-Function Relationship, *J Geophys Res Biogeosci*, 127,
761 <https://doi.org/10.1029/2021JG006748>, 2022.
- 762 Naidoo, L., Mathieu, R., Main, R., Kleyhans, W., Wessels, K., Asner, G., and Leblon, B.: Savannah woody structure
763 modelling and mapping using multi-frequency (X-, C- and L-band) Synthetic Aperture Radar data, *ISPRS Journal of
764 Photogrammetry and Remote Sensing*, 105, 234–250, <https://doi.org/10.1016/j.isprsjprs.2015.04.007>, 2015.
- 765 Pan, J., Zhao, R., Xu, Z., Cai, Z., and Yuan, Y.: Quantitative estimation of sentinel-1A interferometric decorrelation using
766 vegetation index, *Front Earth Sci (Lausanne)*, 10, <https://doi.org/10.3389/feart.2022.1016491>, 2022.
- 767 Perrone, M., Conti, L., Galland, T., Komárek, J., Lagner, O., Torresani, M., Rossi, C., Carmona, C. P., de Bello, F., Rocchini,
768 D., Moudrý, V., Šimová, P., Bagella, S., and Malavasi, M.: “Flower power”: How flowering affects spectral diversity metrics
769 and their relationship with plant diversity, *Ecol Inform*, 81, 102589, <https://doi.org/10.1016/j.ecoinf.2024.102589>, 2024.
- 770 Potapov, P., Li, X., Hernandez-Serna, A., Tyukavina, A., Hansen, M. C., Kommareddy, A., Pickens, A., Turubanova, S., Tang,
771 H., Silva, C. E., Armston, J., Dubayah, R., Blair, J. B., and Hofton, M.: Mapping global forest canopy height through
772 integration of GEDI and Landsat data, *Remote Sens Environ*, 253, 112165, <https://doi.org/10.1016/j.rse.2020.112165>, 2021.



- 773 Qi, J., Chehbouni, A., Huete, A. R., Kerr, Y. H., and Sorooshian, S.: A modified soil adjusted vegetation index, *Remote Sens*
774 *Environ*, 48, 119–126, [https://doi.org/10.1016/0034-4257\(94\)90134-1](https://doi.org/10.1016/0034-4257(94)90134-1), 1994.
- 775 Roberts, D. R., Bahn, V., Ciuti, S., Boyce, M. S., Elith, J., Guillera-Aroita, G., Hauenstein, S., Lahoz-Monfort, J. J., Schröder,
776 B., Thuiller, W., Warton, D. I., Wintle, B. A., Hartig, F., and Dormann, C. F.: Cross-validation strategies for data with temporal,
777 spatial, hierarchical, or phylogenetic structure, *Ecography*, n/a--n/a, <https://doi.org/10.1111/ecog.02881>, 2016.
- 778 Rocchini, D., Thouverai, E., Marcantonio, M., Iannacito, M., Da Re, D., Torresani, M., Bacaro, G., Bazzichetto, M., Bernardi,
779 A., Foody, G. M., Furrer, R., Kleijn, D., Larsen, S., Lenoir, J., Malavasi, M., Marchetto, E., Messori, F., Montagni, A., Moudry,
780 V., Naimi, B., Ricotta, C., Rossini, M., Santi, F., Santos, M. J., Schaepman, M. E., Schneider, F. D., Schuh, L., Silvestri, S.,
781 Šimová, P., Skidmore, A. K., Tattoni, C., Tordoni, E., Vicario, S., Zannini, P., and Wegmann, M.: rasterdiv—An Information
782 Theory tailored R package for measuring ecosystem heterogeneity from space: To the origin and back, *Methods Ecol Evol*,
783 12, 1093–1102, <https://doi.org/10.1111/2041-210X.13583>, 2021.
- 784 Rouse, J. W., Haas, R. H., Schell, J. A., Deering, D. W., and others: Monitoring vegetation systems in the Great Plains with
785 ERTS, *NASA Spec. Publ*, 351, 309, 1974.
- 786 Schneider, F. D., Ferraz, A., Hancock, S., Duncanson, L. I., Dubayah, R. O., Pavlick, R. P., and Schimel, D. S.: Towards
787 mapping the diversity of canopy structure from space with GEDI, *Environmental Research Letters*, 15,
788 <https://doi.org/10.1088/1748-9326/ab9e99>, 2020.
- 789 Schwartz, M., Ciais, P., Ottlé, C., De Truchis, A., Vega, C., Fayad, I., Brandt, M., Fensholt, R., Baghdadi, N., Morneau, F.,
790 Morin, D., Guyon, D., Dayau, S., and Wigneron, J.-P.: High-resolution canopy height map in the Landes forest (France) based
791 on GEDI, Sentinel-1, and Sentinel-2 data with a deep learning approach, *International Journal of Applied Earth Observation*
792 *and Geoinformation*, 128, 103711, <https://doi.org/10.1016/j.jag.2024.103711>, 2024.
- 793 Shendryk, Y.: Fusing GEDI with earth observation data for large area aboveground biomass mapping, *International Journal of*
794 *Applied Earth Observation and Geoinformation*, 115, 103108, <https://doi.org/10.1016/j.jag.2022.103108>, 2022.
- 795 Shimada, M., Itoh, T., Motooka, T., Watanabe, M., Shiraishi, T., Thapa, R., and Lucas, R.: New global forest/non-forest maps
796 from ALOS PALSAR data (2007–2010), *Remote Sens Environ*, 155, 13–31, <https://doi.org/10.1016/j.rse.2014.04.014>, 2014.
- 797 Shugart, H. H., Saatchi, S., and Hall, F. G.: Importance of structure and its measurement in quantifying function of forest
798 ecosystems, *J Geophys Res Biogeosci*, 115, <https://doi.org/10.1029/2009JG000993>, 2010.
- 799 Sothe, C., Gonsamo, A., Lourenço, R. B., Kurz, W. A., and Snider, J.: Spatially Continuous Mapping of Forest Canopy Height
800 in Canada by Combining GEDI and ICESat-2 with PALSAR and Sentinel, *Remote Sens (Basel)*, 14, 5158,
801 <https://doi.org/10.3390/rs14205158>, 2022.
- 802 Sun, J., Yu, X., Wang, H., Jia, G., Zhao, Y., Tu, Z., Deng, W., Jia, J., and Chen, J.: Effects of forest structure on hydrological
803 processes in China, *J Hydrol (Amst)*, 561, 187–199, <https://doi.org/10.1016/j.jhydrol.2018.04.003>, 2018.
- 804 Taddeo, S., Dronova, I., and Harris, K.: Greenness, texture, and spatial relationships predict floristic diversity across wetlands
805 of the conterminous United States, *ISPRS Journal of Photogrammetry and Remote Sensing*, 175, 236–246,
806 <https://doi.org/10.1016/j.isprsjprs.2021.03.012>, 2021.



- 807 Toda, M., Knohl, A., Luysaert, S., and Hara, T.: Simulated effects of canopy structural complexity on forest productivity, *For*
808 *Ecol Manage*, 538, 120978, <https://doi.org/10.1016/j.foreco.2023.120978>, 2023.
- 809 Tuanmu, M. and Jetz, W.: A global, remote sensing-based characterization of terrestrial habitat heterogeneity for biodiversity
810 and ecosystem modelling, *Global Ecology and Biogeography*, 24, 1329–1339, <https://doi.org/10.1111/geb.12365>, 2015.
- 811 Valbuena, R., O’Connor, B., Zellweger, F., Simonson, W., Vihervaara, P., Maltamo, M., Silva, C. A., Almeida, D. R. A.,
812 Danks, F., Morsdorf, F., Chirici, G., Lucas, R., Coomes, D. A., and Coops, N. C.: Standardizing Ecosystem Morphological
813 Traits from 3D Information Sources, *Trends Ecol Evol*, 35, 656–667, <https://doi.org/10.1016/j.tree.2020.03.006>, 2020.
- 814 Vollrath, A., Mullissa, A., and Reiche, J.: Angular-Based Radiometric Slope Correction for Sentinel-1 on Google Earth Engine,
815 *Remote Sens (Basel)*, 12, 1867, <https://doi.org/10.3390/rs12111867>, 2020.
- 816 Zhai, L., Will, R. E., and Zhang, B.: Structural diversity is better associated with forest productivity than species or functional
817 diversity, *Ecology*, 105, <https://doi.org/10.1002/ecy.4269>, 2024.
- 818